Smart Structures and Systems, *Vol. 28, No. 6 (2021) 761-777*
https://doi.org/10.12989/sss.2021.28.6.761

Piezoelectric skin sensor for electromechanical impedance responses sensitive to concrete damage in prestressed anchorage zone

Ngoc-Loi Dang [a], Quang-Quang Pham [b] and Jeong-Tae Kim*

Department of Ocean Engineering, Pukyong National University, 45 Yongso-ro, Nam-gu, Busan 48513, Republic of Korea

(*Received November 30, 2020, Revised September 3, 2021, Accepted September 6, 2021*)

Abstract. This study presents a numerical investigation on the sensitivity of electromechanical (EM) impedance responses to inner damaged concrete of a prestressed anchorage zone. Firstly, the Ottosen yield criterion is selected to simulate the plasticity behavior of the concrete anchorage zone under the compressive loading. Secondly, several overloading cases are selected to analyze inner damage formations in the concrete of the anchorage zone. Using a finite element (FE) model of the anchorage zone, the relationship between applied forces and stresses is analyzed to illustrate inner plasticity regions in concrete induced by the overloading. Thirdly, EM impedance responses of surface-mounted PZT (lead-zirconate-titanate) sensors are numerically acquired before and after concrete damage occurrence in the anchorage zone. The variation of impedance responses is estimated using the RMSD (root-mean-square-deviation) damage metric to quantify the sensitivity of the signals to inner damaged concrete. Lastly, a novel PZT skin, which can measure impedance signatures in predetermined frequency ranges, is designed for the anchorage zone to sensitively monitor the EM impedance signals of the inner damaged concrete. The feasibility of the proposed method is numerically evaluated for a series of damage cases of the anchorage zone. The results reveal that the proposed impedance-based method is promising for monitoring inner damaged concrete in anchorage zones.

Keywords: anchorage zone; concrete damage; electromechanical impedance; piezoelectric skin sensor; prestressed concrete structure

1. Introduction

Prestressed concrete (PSC) has been widely used as a cost-effective way for bridge construction. In the PSC bridges, anchorage zones play a critical role in bearing the designed prestressing forces. During long-term services, concrete cracks are routinely observed in the anchorage zone attributed to structural origins (i.e., repeating serve loads, natural disasters) and nonstructural origins (e.g., thermal strains and material degradation). The significance of concrete cracks is an increasing concern for designers and regulators to secure the structural load capacity and durability (Mehrabi *et al*. 2010, Okumus and Oliva 2013, Jang *et al*. 2019). Therefore, the damaged concrete in the critical anchorage member should be monitored to ensure structural integrity and prevent tragic collapses (Putcha *et al*. 2020).

In practice, visual inspection is commonly used to assess the service performance of PSC members by inspecting crack properties (lengths, widths, and patterns) (Lee and Kalos 2014). Although visual inspection can provide much information on the inspected domain, the method is time-consuming and experience-dependent on the estimation and judgment. To overcome the shortcomings, a vision-based technique has been employed for the automatic monitoring of cracks and spalling in bridges (Huynh *et al*. 2019, Jang *et al*. 2020, Kang *et al*. 2020). The emerging method would be efficient for inspection of surface defects based on sufficient training datasets; however, it could not detect invisible defects (i.e., inner cracks) of the inspected structure.

For the last two decades, vibration-based methods have been developed to monitor and localize cracks in PSC structures (Kim and Stubbs 2003, Loutridis *et al*. 2005, Park *et al*. 2007). However, the methods utilize low modal frequencies, which are less sensitive to incipient damages located in prestressed anchorage zones. As a local monitoring way, Grosse (2009) utilized the acoustic emission method to detect damages in a large-scale PSC bridge. Since measured signals consist of various sources of noise (e.g., ambient vibrations), it requires complex algorithms to identify the acoustic emission of the bridge from the measured data. Strain-based methods (Yao *et al*. 2014) have been considered as a simple way to detect cracks using well-defined stress-strain relations. Henault *et al*. (2012) embedded fiber optic sensors to detect the cracks in a reinforced concrete beam. The fabrication of sensing cable-embedded optical fibers remains as a challenge.

Impedance-based techniques have been adopted to monitor the health conditions of various structures (Park *et al*. 2012, Lu *et al*. 2017, Ryu *et al*. 2018, Zhang *et al*. 2020a). As the cost-effective techniques using piezoelectric sensors (e.g., lead-zirconate-titanate (PZT) patches),

*Corresponding author, Professor,
E-mail: idis@pknu.ac.kr
[a] Post-Doctoral Researcher
[b] Ph.D. Student

ISSN: 1738-1584 (Print), 1738-1991 (Online)

electromechanical (EM) impedance responses are measured to quantify their variations for the indication of damage occurrence. The methods utilize high-frequency excitation (e.g., often ultrasonic bands), thus permitting to catch the incipient defects in the inspected structures. Yang *et al*. (2008) and Ai *et al*. (2018) attempted to monitor crack-induced overloading from an array of PZT sensors mounted on concrete structures. Their experimental results revealed that impedance features are promising to detect surface concrete cracking. Also, Zhang *et al*. (2020a) utilized impedance signals measured from smart aggregate (i.e., PZT sensor embedded in protective cover) to monitor stiffness degradation of a compressive concrete member. However, the applicability of an embedded PZT sensor is limited to new PSC structures but not to existing ones.

The anchorage zone of a PSC bridge resists extremely high compressive stresses caused by prestressing installation and also during lifetime service (Breen 1994, Cervenka and Ganz 2014). The anchorage zone could be potentially damaged due to overloaded traffic volume, material degradation, and extreme natural events (e.g., earthquake). The damage in the anchorage zone is often occurred in forms of inner concrete cracks due to eccentric overloads in the bearing plate, which is embedded in the concrete body to transfer the prestressed force from the anchor head to the main structure. To ensure the safety of the anchorage zone, many research attempts have been made to propose new design methods (He and Liu 2010, Hou *et al*. 2017, Xia *et al*. 2020) and new anchorage types (Wu *et al*. 2018, Ro *et al*. 2020). Many studies have also focused on assessing prestressed force or localizing strand breakage in the tendon anchorage (Min *et al*. 2016, Huynh and Kim 2017b, Ryu *et al*. 2018, Dang *et al*. 2019). However, the monitoring of the inner concrete cracks has not been significantly investigated yet via the impedance-based methods. So, it is needed to develop a robust impedance-based method for monitoring the anchorage, which is damaged by inner concrete cracks.

Various research efforts have been made to simulate the inelastic behavior of concrete members. In general, models for concrete can be classified into constitutive models based on plasticity theory (Ottosen and Ristinmaa 2005, Papanikolaou and Kappos 2007), damage models by introducing scalar or tensor damage variables (Lee and Fenves 1998, Dragon *et al*. 2000), and mixed plasticity-damage model (Jefferson *et al*. 2016). Due to brittle materials (e.g., concrete) behaving significantly different in compression and tension, failure criteria for concrete (e.g., Mohr-coulomb criterion or Ottosen criterion) are potentially used (Ottosen and Ristinmaa 2005, Hofstetter 2013, Yaghoubi *et al*. 2014). Among these, the Ottosen criterion can be considered as one of the most successful criteria because it demonstrated a good agreement with the test results of concrete under multiaxial stress states (Ottosen 1977). Recently, elasto-plastic model and an anisotropic damage model (with scalar damage) (Zhang *et al*. 2020b, Vilppo *et al*. 2021) for concrete based on the Ottosen criterion is further developed to better capture damage under various conditions of concrete (e.g., ultrahigh strength of concrete). In numerical analysis, concrete damage (e.g., cracks) representing strain-softening phenomenon is formed based on stress criterion, that is, when tensile or compressive strength is exceeded. For anchorage zones, the allowable stresses head of a bearing plate are varied 1.25-3σ_{ci} (σ_{ci} = 0.75σ_c) (Roberts 1990, AASHTO 2007, Nawy 2010), where σ_{ci} and σ_c are concrete strength of concrete at steel-strand installation and at 28-days. The determination of damage regions based on the limit stresses, which are mostly adopted in concrete damage model, is not feasible. The failure criterion based on the Ottosen model was adopted to simulate stress-strain responses in the prestressed anchorage zone.

In this study, the sensitivity of EM impedance responses to inner damaged concrete of the anchorage zone induced by overloading is numerically investigated. Specifically, studies are needed to quantitatively explain how the PZT sensor should be placed to catch meaningful impedance signatures for the inner damaged concrete of the anchorage zone. Firstly, the Ottosen yield criterion is selected to simulate the plasticity behavior of the concrete anchorage zone under the compressive loading. Secondly, several overloading cases are selected to analyze inner damage formations in the concrete of the anchorage zone. Using a FE model of the anchorage zone, the relationship between applied forces and stresses is analyzed to illustrate inner plasticity regions in concrete induced by the overloading. Thirdly, EM impedance responses of surface-mounted PZT sensors are numerically acquired before and after concrete damage occurrence in the anchorage zone. The variation of impedance responses is estimated using the RMSD damage metric to quantify the sensitivity of the signals to inner damaged concrete. Lastly, a novel PZT skin, which can measure impedance signatures in predetermined frequency ranges, is designed for the anchorage zone to sensitively monitor the EM impedance signals of the inner damaged concrete. The feasibility of the proposed method is numerically evaluated for a series of damage cases of the anchorage concrete zone. The RMSD indices of PZTs' impedance signals are utilized to illustrate damage locations and severity on the anchorage zone.

2. Simulation of inner concrete damage in prestressed anchorage zone

2.1 Ottosen plasticity model for concrete

The Ottosen yield criterion with four parameters is well-known as a plasticity model for the short-time loading of concrete (Ottosen and Ristinmaa 2005). The failure surface has the following characteristics: (1) it deals with the significant difference in tensile and compression behave of concrete; (2) it has a curve shape on the meridian plane, and (3) the shape is slightly changed from triangular to round under increasing hydrostatic pressure on the deviatoric plane. The Ottosen criterion yielded a good agreement with test results for different states of stresses of concrete members (e.g., biaxial compressive stress).

The failure surface of concrete based on the Ottosen criterion is defined:

$$A\frac{J_2}{\sigma_c}+\lambda(\theta)\sqrt{J_2}+BI_1-\sigma_c=0 \tag{1}$$

$$\lambda(\theta)=k_1\cos\left(\frac{1}{3}\arccos(k_2\cos 3\theta)\right) \quad \cos 3\theta\geq 0 \tag{2}$$

$$\lambda(\theta)=k_1\cos\left(\frac{\pi}{3}-\frac{1}{3}\arccos(-k_2\cos 3\theta)\right) \quad \cos 3\theta<0 \tag{3}$$

where A, B, k_1, and k_2 are dimensionless parameters of the concrete. The parameter k_1 is the size factor; k_2 is the shape factor bounded from $0 \leq k_2 \leq 1$; σ_c is the uniaxial compression strength of concrete; I_1 is the first invariant of the stress tensor $\boldsymbol{\sigma}$. Also, J_2 is the second invariant of the deviatory stress tensor $\boldsymbol{s} = \boldsymbol{\sigma} - \sigma_m\boldsymbol{I}$, in which σ_m is the averaged normal stress ($\sigma_m = I_1/3$). The θ is the stress angle on the deviatoric plane defined based on the second (J_2) and third invariant (J_3 = det(**s**)) invariants of the deviatoric stress tensor, as follows

$$\theta=\frac{1}{3}\arccos\left(\frac{3\sqrt{3}}{2}\frac{J_3}{J_2^{1.5}}\right) \tag{4}$$

The four parameters A, B, k_1, and k_2 can be determined from experimental measurements using different stress states, including (s1) uniaxial tensile strength σ_t, (s2) uniaxial compressive strength σ_c, (s3) equibiaxial compressive strength σ_{bc}, and (s4) a failure stress state on the compressive meridian (I_1, $\sigma_e = \sqrt{3J_2}$). The states s1 and s3 lie on the tensile meridian, and states s2 and s4 lie on the compressive meridian. It is obvious that the Ottosen yield criterion is equivalent to the Drucker-Prager criterion when $A = 0$ and $\lambda(\theta)$ = constant (Alejano and Bobet 2012). Also, it is equal to the Von Mises criterion when $A = B = 0$ and $\lambda(\theta)$ = constant (Alejano and Bobet 2012).

By substituting the four points of failure stress states (s1-s4), the four parameters A, B, k_1, and k_2 can be determined as functions of σ_{bc}/σ_c, σ_t/σ_c, and, $I_1, \sqrt{3J_2}$ (Yaghoubi *et al*. 2014). Using the experimental results by Kuper (Kupfer *et al*. 1969), that is, $\sigma_{bc}/\sigma_c = 1.16$, $I_1 = -2.887\sigma_c$, $\sigma_e = 4.899\sigma_c$, the tensile strength of concrete σ_t was taken as 10% the compressive strength σ_c (i.e., $\sigma_t/\sigma_c = 0.1$), the four parameters of Ottosen yield criterion for concrete (Ottosen and Ristinmaa 2005, Yaghoubi *et al*. 2014) was determined as: A = 1.267; B = 3.196; k_1 = 11.736, and k_2 = 0.980. Furthermore, Fig. 1 shows the Ottosen failure surface on the π-plane (see Fig. 1(a)) and in plane stress (see Fig. 1(b)) for $\sigma_{bc}/\sigma_c = 1.16$, $\sigma_t/\sigma_c = 0.1$, $\sigma_m = I_1/3, \sigma_e = \sqrt{3J_2}$, in which σ_e is the effective stress.

2.2 Finite element model of prestressed anchorage zone

As shown in Fig. 2, a 9-strand anchorage zone was selected as a target structure to simulate damage formation of inner concrete in the anchorage zone. The geometric parameters were selected based on the real design of the I-girder bridge (Chauthoi620 2018). The anchorage zone consists of a 9-strand anchor head (a diameter of ϕ159 mm and height of 75 mm) with wedges, a bearing plate ($a \times a \times t_b$ = 210 × 210 × 35 mm), and a concrete block (length × width × height = L × W × B). For the symmetric anchorage zone, the considered length L of the concrete block should be selected at least twice distances from the center of anchorage to the edge of concrete block (see Fig. 2(a)) (Guyon 1974, Breen 1994). In the anchorage zone (L < W), stress-strain responses are disturbed, and they are almost linear distribution at the anchorage end (L ≥ W). For the 9-strand anchorage, the size of the concrete block was selected as L × W × B = 500 × 500 × 500 mm.

A duct (ϕ120 mm) was placed at the center of the concrete block for passing prestressing strands (see Fig. 2(a)). The reinforcement for the concrete consists of a spiral, orthogonal stirrups, and reinforcing frame (VSL 2018). The volume ratio of reinforcement (steel rebars) to concrete block was about 2.8%. The anchorage zone was designed to permanently resist a total compressive force of 1170 kN induced by P = 130 kN per strand. Each steel strand had ϕ15.2 mm in diameter, tensile strength f_u = 1860 MPa, and breaking load P_k = 260 kN (VSL 2018).

For the analysis of impedance responses, the rebar was converted to concrete using the equivalent Young modulus, and simulated materials were assumed as elastic homogeneous mediums (Ai *et al*. 2019). To gain impedance signals from the interactions between PZT-anchorage, at first, the structural analysis was conducted to illustrate

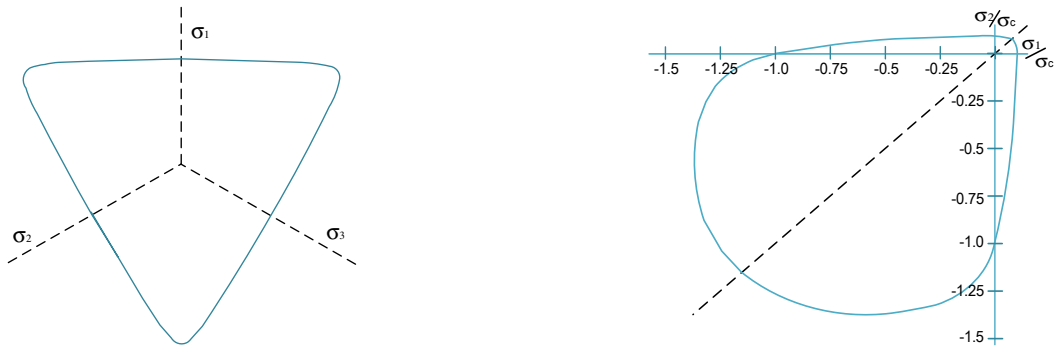

(a) π-plane (b) Plane stress

Fig. 1 Failure surface-based Ottosen criterion with four parameters

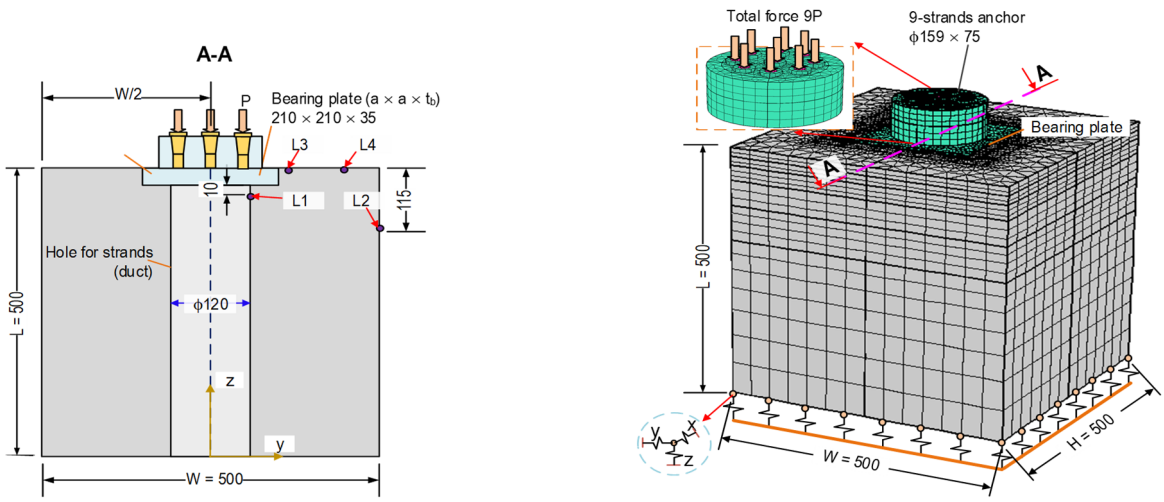

(a) Cross-section A-A (b) 3D view of anchorage zone

Fig. 2 FE model of prestressed anchorage zone, unit in mmm

Table 1 Material properties of anchorage zone components

Parameters	Anchorage system	Pure concrete	Steel bars
Young's modulus, E (GPa)	200	29.9	200
Poisson's ratio, ν	0.33	0.2	0.33
Mass density, ρ (kg/m^3)	7850	2400	7850
Compressive strength, (MPa)	460	35	460
Tensile strength, (MPa)	460	3.5	460

potential damage zones in the anchorage. Then, the impedance analysis was performed to acquire the signals for different damage levels.

The material properties of the anchorage zone components were listed in Table 1. The compressive strength of pure concrete was selected as σ_c = 35 MPa with $\sigma_t = 0.1\sigma_c$. For the FE analysis, the reinforcement and the concrete were converted into a simplified model by an equivalent elastic modulus, as shown in Eq. (5)

$$E_{eq} = \frac{V_s}{V_t}E_s + \frac{V_c}{V_t}E_c \quad (5)$$

where E_s, E_c, and E_{eq} are the elastic moduli of the reinforcement, the pure concrete, and the equivalent reinforced concrete, respectively. Also, V_s, V_c, and V_t are the volumes of the reinforcement, the pure concrete, and the equivalent reinforced concrete, respectively.

The volumes and Young's moduli of the anchorage components were listed in Table 2. The equivalent elastic modulus, E_{eq} (34.54 GPa), was about 15.5% larger than that of the pure concrete (E_c = 29.9 GPa). Moreover, the compressive strength of the equivalent concrete could be computed based on the elastic modulus (AASHTO 2007)

$$\sigma_c^{eq} = \left(\frac{E_{eq}}{0.043 \times \rho^{1.5}}\right)^2 \quad (6)$$

By substituting E_{eq} and ρ into Eq. (6), the compression strength and the tensile strength were yielded as $\sigma_c^{eq} = 46.5\,MPa$ and $\sigma_t^{eq} = 4.65\,MPa$, respectively. By considering reinforcement of the anchorage zone, the compressive strength of concrete was increased about 32% compared to the one of pure concrete.

The FE model should be properly meshed to reduce computational cost and minimize numerical error-induced meshing. The try-and-error method based on differences in stress variation under prestress force was utilized to select mesh size for elements. As shown in Fig. 2(b), three-dimensional (3D) elements were modeled for the bearing plate, anchor head with wedges, and the concrete block. The FE model had a total of 48309 elements, including 3282 elements for the anchor head, 1224 elements for the bearing plate, and 43803 elements for the concrete block. The quadratic hexahedral elements were used for the wedges, and the quadratic tetrahedral elements were used for the remaining elements in the FE model. To simulate the remaining part of the structure (i.e., I-girder bridge), the 3D spring elements with $k_x = k_y = 0.5k_z$ were assigned to the bottom surface of the concrete block (Huynh and Kim 2017a, Dang *et al*. 2019). It is noted that the spring stiffness is spring constant per unit area, which is supported by the Comsol Multiphysics tool. Since we focused on analyzing the anchorage-zone responses (i.e., stress/strain and impedance), the value of the spring constant was selected, so that the effect of spring stiffness on anchorage responses under the prestress variation was ignored. After try-and-error procedure, the spring constant was selected as $k_x = k_y = 0.5k_z = 2.5 \times 10^{15}$ (N/m/m^2).

To introduce damage in the anchorage zone, the prestress force was simulated by assigning forces in wedges' surfaces (Bastien *et al*. 2007, Abdullah *et al*. 2015). The prestress force P (total force of 9P) was increased from 0 to 2P (i.e., 0 ~ 2340 kN for the nine strands) via multiple intervals of increment. The nonlinear behavior of the anchorage zone was analyzed by the Ottosen yield criterion. The relationship between stress versus force P was analyzed for the four points L1-L4 of the inner anchorage zone (see

Table 2 Equivalent elastic modulus of reinforced anchorage zone

Parameters	Volume (dm^3)			Elastic modulus (GPa)		
	V_s	V_c	V_t	E_s	E_c	E_{eq}
Value	2.8	97.1	99.9	200	29.9	34.5

Fig. 2(a)).

2.3 Analysis of anchorage zone's responses under overloading

2.3.1 Stress responses in anchorage zone

Fig. 3(a) shows the Von Mises stress of the anchorage under the prestress force P. The maximum stress was occurred up to 310 MPa at the interface between the anchor-bearing plates. Then the stress was reduced to nearly uniform stress (6.12 MPa) at the anchorage end (z = 0). For the centric anchorage zone, it is subjected to three levels of stresses (Nawy 2010), corresponding to Zones 1-3, as shown in Fig. 3(b). In Zone 1, high bearing stress occurred ahead of the anchor plate (the point L1). In Zone 2, tensile-bursting stress occurred normal to the z-axis (the point L2). In Zone 3, high compressive stress occurred beside the bearing plate (the point L3), and also tensile spalling stress occurred at the point L4.

As shown in Figs. 4(a)-(d), the relationships between the prestress force P and the three normal stress components (σ_{xx}, σ_{yy}, and σ_{zz}) were examined at the point L1 (Zone 1), the point L2 (Zone 2), and the points L3-L4 (Zone 3), respectively. At the point L1 (Zone 1), the axial compressive stress (i.e., σ_{zz}) yielded the most significant value, and the stress still increased after reaching the compressive strength $\sigma_c^{eq} = 46.5\ MPa$ (see Fig. 4(a)). At the point L2 (Zone 2), the lateral tensile stress was kept as constant ($\sigma_t^{eq} = 4.65\ MPa$) for a force larger than 1.7P (see Fig. 4(b)). At the point L3 (Zone 3), the compressive stress became nonlinear for a force larger than 1.2P (see Fig. 4(c)). At the point L4 (Zone 3), the tensile stress became nonlinear for a force larger than 1.7P (see Fig. 4(d)).

(a) Von Mises stress under force P (b) Stress contours

Fig. 3 Stress distribution in prestressed anchorage zone

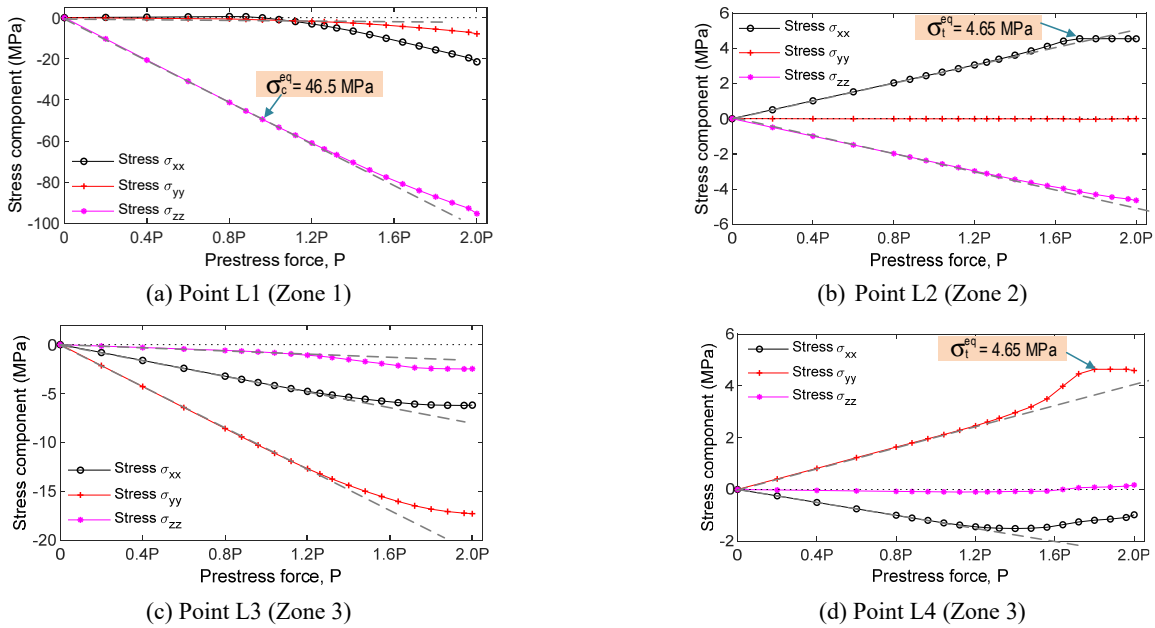

(a) Point L1 (Zone 1) (b) Point L2 (Zone 2)

(c) Point L3 (Zone 3) (d) Point L4 (Zone 3)

Fig. 4 Stress responses versus prestress force P in prestressed anchorage zone

2.3.2 Analysis of inner concrete damage formation due to overloading

It is well-known that the allowable bearing stresses ahead of the bearing plate of the anchorage zone are varied from 1.25-3σ_{ci} (Roberts 1990, AASHTO 2007, Nawy 2010), in which σ_{ci} ($\approx 0.75\sigma_c$) is the compressive strength of concrete at prestressing installation. Moreover, the stresses depend on many parameters, such as geometric quantities of anchor devices, concrete strength, and reinforcement. Based on the Ottosen failure criterion (Ottosen and Ristinmaa 2005), concrete could be damaged under compression, tension, or compression-tension, resulting in difficulties for the determination of damaged regions using limited stress.

It is generally accepted that the ultimate compressive strain yielding concrete damage was varied 1.8-2.4 $\times$ 10^{-3} mm/mm for normal concrete (σ_c < 60 MPa) (Schneider 1976, Chang *et al*. 2006, Darwin *et al*. 2016). As observed in Fig. 4, the stress distributions were varied on the axial and lateral components, and their allowable stresses were different for Zones 1-3. In this analysis, the ultimate strain was selected as $\sigma_c = 2\times10^{-3}$ mm/mm (compressive damage) and $\sigma_t = 0.1\sigma_c$ (tensile damage). In other words, when a region had strain larger than the ultimate strain, it could be considered as the damaged region.

Figs. 5(a)-(c) show strain distributions in the anchorage zone under the prestressing force 1.6P for axial strain, axial-plastic strain, and lateral-plastic strain, respectively. The axial compressive strain got a maximum value (~2.7 $\times$ 10^{-3} mm/mm) in Zone 1 (see Fig. 5(a)). For axial direction, the tensile plastic strain occurred in Zone 3, and the compressive plastic strain occurred in Zone 1 (see Fig. 5(b)). For the lateral direction, the tensile plastic strain only occurred in Zone 1 (see Fig. 5(c)). Thus, the incipient concrete damage potentially occurred in Zone 1 and Zone 3.

As shown in Fig. 6 and listed in Table 3, the ultimate strains (i.e., σ_c and σ_t) were applied for Zones 1-3 to classify damaged and undamaged regions under the four prestress force levels. The damage volume ratio (DVR) was defined as a ratio of the damaged concrete volume to the one of the anchorage zone. In the intact case, there was no damage under the prestress force P (1170 kN for 9-strands). In damage case 1, the incipient spalling damage (a damaging size of about 50 $\times$ 14 $\times$ 2.5 mm corresponding to width $\times$ height $\times$ thickness) was occurred with DVR = 0.01% at the inner concrete of Zone 3 when the prestress force was increased to 1.2P (see Fig. 6(b)). In damage case

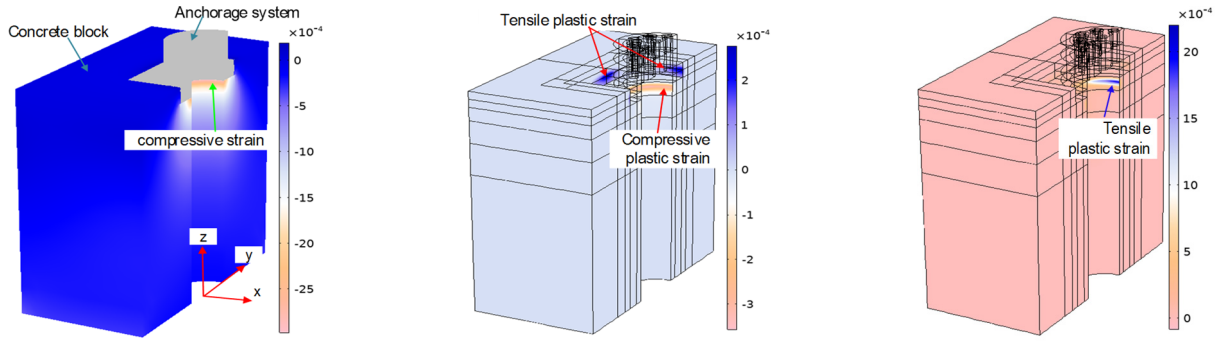

(a) Axial strain (b) Axial plastic strain (c) Lateral plastic strain

Fig. 5 Strain distributions in anchorage zone under prestress force 1.6P

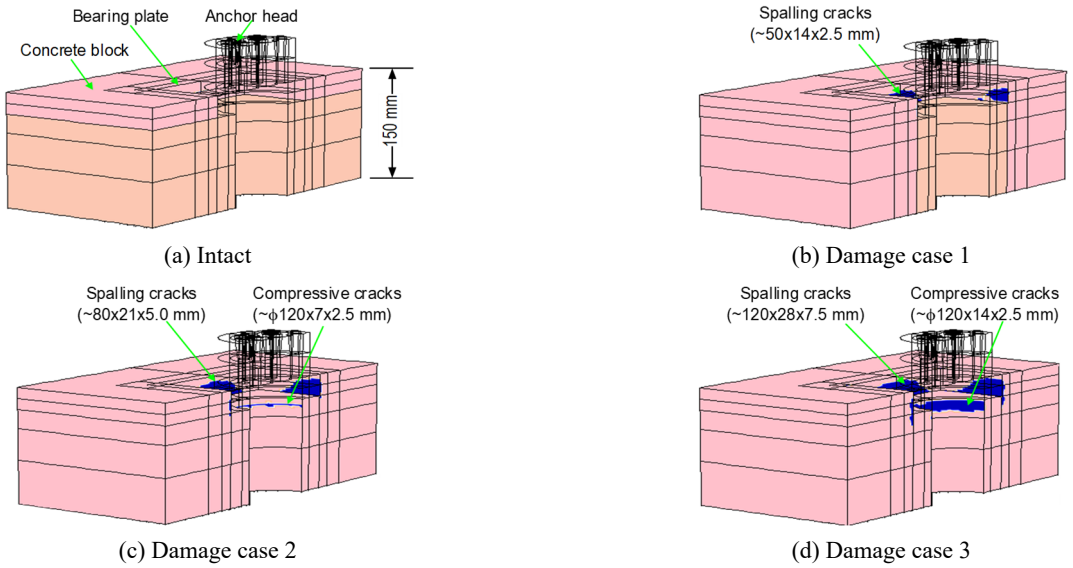

(a) Intact (b) Damage case 1

(c) Damage case 2 (d) Damage case 3

Fig. 6 Damaged regions in concrete of anchorage zone induced by overloading

Table 3 Damage simulation cases by overloading in anchorage zone

Scenarios	Prestress force (kN)		Description of damage severity
	1 strand	9 strands	
Intact	P*	1170	Undamaged
Damage case 1	1.2P	1404	Incipient damage occurred inner concrete surrounding the bearing plate with DVR = 0.01%.
Damage case 2	1.4P	1638	The damage was propagated, and incipient damage occurred ahead of bearing plate with DVR = 0.034%.
Damage case 3	1.6P	1872	The inner damages were propagated with DVR = 0.12%.

*Total force was 9P with P = 130 kN for a strand

2, the damage in Zone 3 was propagated, and the incipient damage (a size of ϕ120 × 7 × 2.5 mm corresponding to diameter × height × thickness) occurred with DVR = 0.034% at Zone 1 when the prestress force was increased to 1.4*P* (see Fig. 6(c)). In damage case 3, the damages were propagated to DVR = 0.12% when the prestress force was increased to 1.6*P* (see Fig. 6(d)).

3. Sensitivity of impedance responses to inner concrete damage

3.1 Impedance-based damage detection method

Using the dual effects of piezoelectric materials (e.g., lead zirconate titanate, PZT), Liang *et al*. (1996) proposed the concept of the electromechanical-mechanical impedance method. In the method, a PZT patch was surface-mounted onto an inspected structure to acquire EM impedance responses from coupling interactions between the PZT patch-structure under harmonic excitation. In practice, the electric current $I(\omega)$ was measured and utilized to calculate EM impedance responses (Liang *et al*. 1996)

$$Z(\omega) = \frac{V(\omega)}{I(\omega)} = \left\{ i\omega A_p \left[\hat{\varepsilon}_{33}^{T} - \frac{1}{\frac{Z_a(\omega)}{Z_s(\omega)} + 1} d_{3x}^2 \hat{Y}_{xx}^{E} \right] \right\}^{-1} \quad (7)$$

where $\hat{Y}_{xx}^{E}$, $\hat{\varepsilon}_{xx}^{T}$, and d_{3x} are respectively the complex Young's modulus of the PZT patch, the complex dielectric constant, and the piezoelectric coupling constant in the x-direction at zero stress; and A_p is the geometric constants of the PZT patch. The parameters η and δ are structural damping loss factor and dielectric loss factor of the piezoelectric patch. $Z_a(\omega)$ and $Z_s(\omega)$ are structural-mechanical impedance of the PZT sensor and that of the host structure, separately. The structural impedance depends on the structural properties of the monitored structure

$$Z_s(\omega) = c + m\frac{\omega^2 - \omega_n^2}{\omega} i \quad (8)$$

where c and m are the damping coefficient and the mass of the structure, respectively; ω_n, and ω are the natural frequency of the structure and the excitation voltage. It is obvious that the EM impedance as a function of dynamic parameters of both the PZT sensor and the monitored structure. When the mechanical and electrical material properties of the PZT sensor are constants, any changes in structural properties (e.g., concrete damage) can be represented by changes in impedance signals.

To analyze the sensitivity of impedance signals, the RMSD (root mean square deviation) damage metric (Yang *et al*. 2008) is commonly employed

$$RMSD(Z, Z^*) = \sqrt{\sum_{i=1}^{n} [Z^*(\omega_i) - Z(\omega_i)]^2 / \sum_{i=1}^{n} Z(\omega_i)^2} \quad (9)$$

where $Z(\omega_i)$ and $Z^*(\omega_i)$ are the real components of the impedance signatures measured before and after the concrete damage of the i^{th} frequency, respectively, and n denotes the number of frequency points in the sweeping band.

3.2 FE analysis of prestressed anchorage zone with PZT sensor

FE analyses were performed using Comsol Multiphysics to analyze the sensitivity of impedance responses to inner damaged concrete. A series of FE models were established for the intact and three damage cases of the anchorage zone (see Table 3). In this analysis, the damaged elements were simulated by removing Young's modulus up to 1%. It is noted that Young's modulus decreased when concrete is damaged, thus resulting in a modification in structural stiffness (Mazars and Pijaudier-Cabot 1989, Zhao *et al*. 2019).

Figs. 7(a)-(c) illustrate the locations and shapes of the simulated damage elements in the FE models for the damage cases 1-3, respectively. In damage case 1, damaged elements had a size of 50 × 14 × 2.5 mm, and its distance from the concrete top was 21 mm (see Fig. 7(a)). In damage case 2, the damaged elements had a size of 80 × 21 × 5.0 mm (14 mm from the concrete top), and the other had a size of ϕ120 × 7 × 2.5 mm (beneath the bearing plate). In damage case 3, the damaged elements were larger than those in damage case 2, and they were also inner concrete (see Fig. 7(c)).

Fig. 8 shows the meshed FE model of the anchorage zone mounted with PZT A (at the middle of the bearing plate) and PZT B (at the corner edge of the bearing plate). The discrimination includes 71570 elements (128 elements for PZTs A&B, 9184 elements for the anchorage system, and 62258 elements for the concrete block). The quadratic

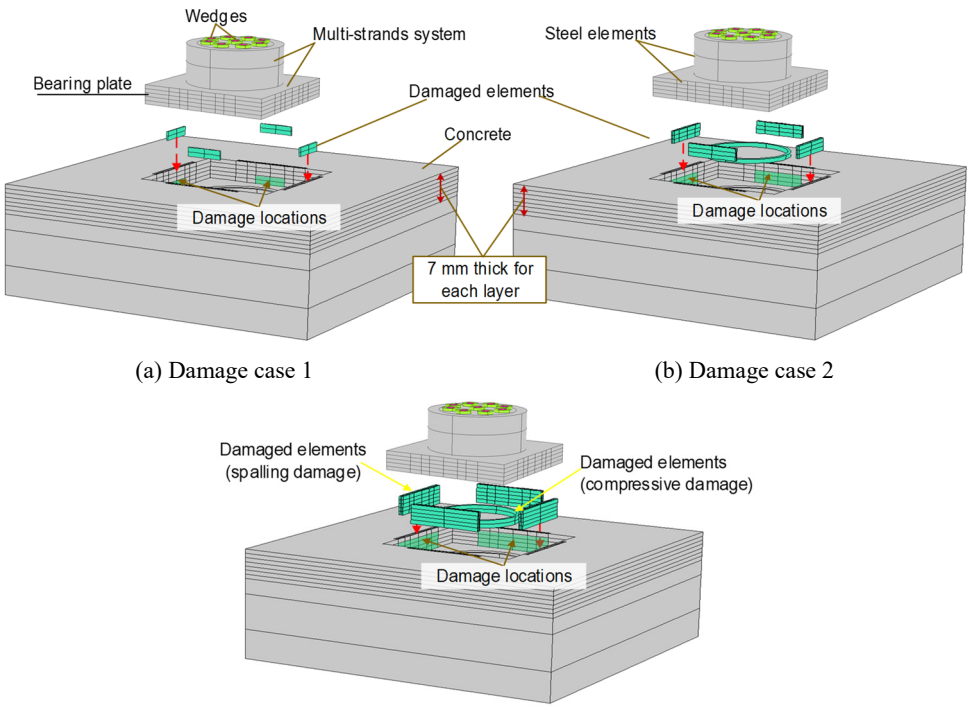

(a) Damage case 1 (b) Damage case 2

(c) Damage case 3

Fig. 7 Locations and shapes of damaged elements in FE model of anchorage zone

hexahedral elements were used for the wedges and the two PZT patches. Moreover, the quadratic tetrahedral elements were used for the concrete block, the bearing plate, and the anchor head. Also, the meshing grids of the damaged elements and the PZT patches were zoomed in Fig. 8(b). As described in Section 2.2, the 3D-spring constants ($k_x = k_y = 0.5k_z = 2.5 \times 10^{15}$ N/m/m^2) were assigned at the bottom surface of the concrete block to simulate the remaining part of the structure.

The PZT 5A with the size of 15 × 15 × 0.51 mm was used to acquire impedance responses. The material properties of the PZT 5A were defined as follows: Young's modulus E = 62.1 GPa; mass density ρ = 7750 kg/m^3; dielectric constant $\varepsilon^T_{33} = 1.53 \times 10^{-8}$ Farad/m; coupling constant $d_{31} = -1.71 \times 10^{-10}$ m/V; damping and dielectric loss factor $\eta = 0.0125$ and $\delta = 0.015$ (Dang *et al*. 2019).

3.3 Sensitivity of impedance responses of surface-mounted PZT sensors to inner concrete damage

3.3.1 Impedance responses of surface-mounted PZT sensors

For the attachment method of the PZT sensor, the determination of a sensitive frequency range can be conducted by the try-and-error method (Kim *et al*. 2010) or selected based on measured ranges of a similar structure. For concrete structures, the first resonant was about 200 kHz (Ai *et al*. 2018, Zhao *et al*. 2019). In this analysis, the frequency range 100-450 kHz was selected to analyze impedance responses-induced concrete damage.

For the intact and three damage cases, impedance signatures were numerically acquired from PZTs A and B

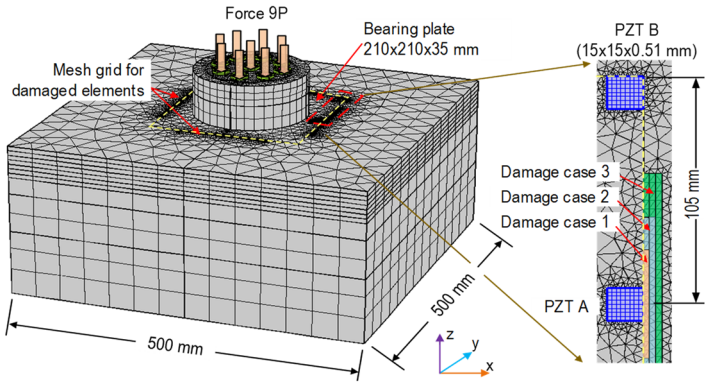

(a) Anchorage zone with PZT sensors (b) Position of PZT sensors

Fig. 8 FE model of anchorage zone with surface-mounted PZT sensors

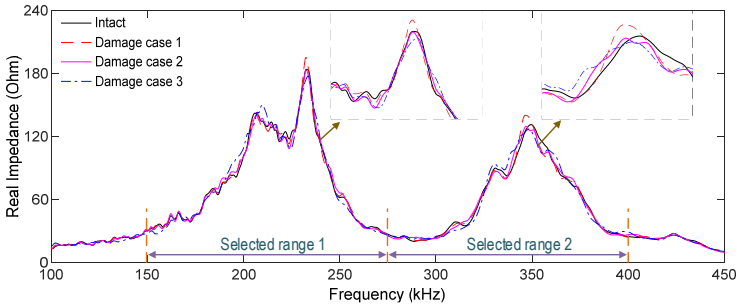

(a) PZT A (middle edge of bearing plate)

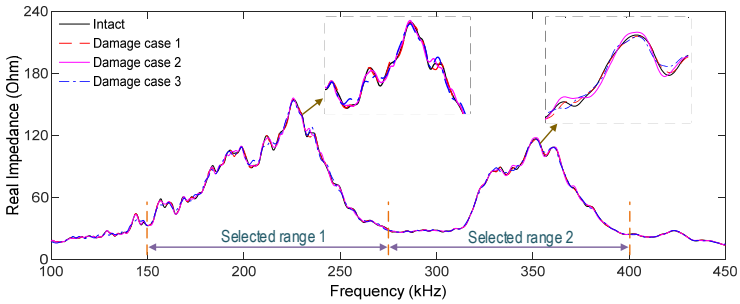

(b) PZT B (corner edge of bearing plate)

Fig. 9 Impedance responses of surface-mounted PZT sensors

for the frequency range of 100-450 kHz with 451 measured points (an interval of 1.0 kHz) using 1V harmonic excitation. As shown in Fig. 9, impedance signals of PZT A were relatively sensitive to the inner concrete damage as compared to those of PZT B. The impedance responses were analyzed in the two resonant frequency ranges, which were 150-275 kHz (Range 1) and 275-400 kHz (Range 2). It is known that the resonant impedance frequencies contain meaningful structural information (Yang *et al*. 2008, Dang *et al*. 2019). Thus, Ranges 1-2 of impedance were selected for the impedance-based concrete damage detection.

3.3.2 Impedance-based detection result of inner concrete damage

The RMSD damage index was used to quantify variations of impedance signatures for Ranges 1 and 2. Fig. 10 shows damage detection results using impedance features of PZT A (which was placed at the middle edge of the bearing plate) and PZT B (which was placed at the corner edge of the bearing plate). The magnitudes of the RMSD index were gradually increased for the three damage cases. The RMSD magnitudes of PZT A were relatively higher than those of PZT B. It is noted that PZT A was mounted close to the damaged concrete. For the PZT A, furthermore, the RMSD indices of Range 2 were slightly higher than those of Range 1 (see Fig. 10(a)). This is contrary to the sensitivity of PZT B's impedance feature, which was Range 1 more sensitive than Range 2.

3.3.3 Discussion on sensitivity of impedance responses to inner concrete damage

It is well known that more stress variation yielded more changes in impedance signatures (Lim and Soh 2012, Dang *et al*. 2020a). As previously explained, the region of damaged concrete was simulated by reducing Young's modulus of concrete, thus resulting in stress redistribution in the nearby locations (Eringen *et al*. 1977). As a result, the impedance features of PZT A yielded higher sensitivity than those of PZT B.

The sensitivity of impedance responses to inner concrete damage was analyzed as follows. Firstly, the impedance responses acquired by the surface-mounted PZTs were

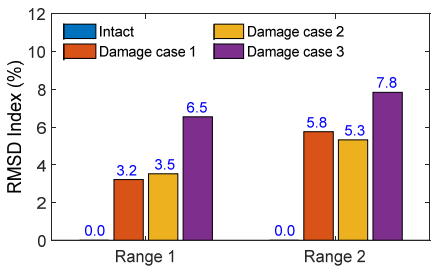

(a) PZT A (middle edge)

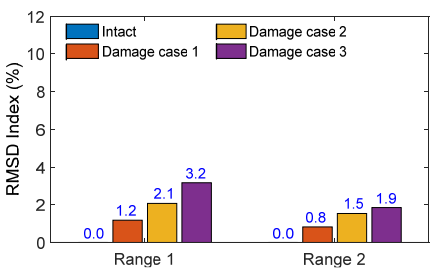

(b) PZT B (corner edge)

Fig. 10 Sensitivity of impedance responses obtained from surface-mounted PZT sensors

relatively changed due to the extent of inner concrete damage. Secondly, the sensitivity of the PZTs' impedance signals was reduced depending on relative distances between the PZTs and the concrete damage locations. Thirdly, the accuracy of damage detection relied on the choice of the selected frequency bands.

It is observed from the analysis that the selection of appropriate frequency bands is crucial to secure the accuracy of the impedance-based damaged detection in the anchorage. Hence, there exists a demand to develop an alternative method to sensitively catch impedance responses-induced concrete damage in the prestressed anchorage zone.

4. PZT skin for inner damaged concrete detection

4.1 Prototype design of PZT skin

Previous studies (Huynh *et al*. 2015, Huynh and Kim 2017b, Dang *et al*. 2020b) show that the sensitive frequency bands of PZT's impedance could be predetermined and enhanced when the impedance signatures were measured via the interface device. In this study, the design parameters of the PZT skin were selected, as illustrated in Figs. 10(a)-(c).

As shown in Fig. 11(a), a circular skin (which is a PZT interface device) with multiple PZT sensors was designed to detect concrete damage in the anchorage. The prestressed anchorage zone consisted of the anchor block, bearing plate, and concrete block. The PZT skins were mounted on the symmetric anchorage system. Total 24 PZTs (8 PZTs in Group A and 16 PZTs in Group B) were placed in the circular skins.

As shown in Fig. 11(b), a quarter of the PZT skin was embedded with six PZT sensors, including two PZTs 1-2 (Group A) and four PZTs 3-6 (Group B). As also highlighted in Fig. 11(b), Region A (for PZTs in Group A) and Region B (for PZTs in Group B) had the same geometric parameters of the PZT skin. In each group, the PZT sensors were equally placed with respect to the anchor head.

As shown in Fig. 11(c), the PZT skin was designed with deformable parts and bonded parts. The deformable parts generated impedance signals from the attached PZT patches in the range of predetermined frequency bands; meanwhile, the bonded parts interacted with the anchorage to locally transmit the change in mechanical behaviors. Therefore, impedance signals can be measured in predetermined frequency ranges based on the dynamic properties of the PZT skin. The prototype of the PZT skin had the following specifications. A bonded section had the inner diameter ϕ_{in} (i.e., the diameter of the anchor head), outer diameter ϕ_{out}, and thickness T_b. A flexible section had a square shape $W_f \times W_f$ and thickness T_f. For region A, its length was limited by an angle α, a width W ($W = W_{b1} + W_f + W_{b2}$). For Region B, its length was limited by an angle β, a width W (see Figs. 11(b)-(c)). PZT sensors were designed with a length L_p, a width W_p, and a thickness T_p. The mobility is the major advantage of the PZT skin technique, thus allowing the applicability into existing structures. Furthermore, since PZT sensors are protected by the skin, it could minimize the effects of external excitations and environmental changes on impedance responses.

4.2 Predetermination of frequency range for PZT skin

Impedance responses of a PZT skin should be analyzed for predetermining its frequency ranges. Geometric parameters of the skin were selected for the 9-strands anchorage zone. The bonded section had ϕ_{in} = 159 mm, ϕ_{out} = 459 mm, and T_p = 2.0 mm. The flexible section had $W_f \times W_f$ = 25 × 25 mm and T_f = 0.7 mm. The PZT patch was $W_p \times L_p \times T_p$ = 15 × 15 × 0.51 mm. For Region A, a segmental PZT skin had α = 45° and W = 75 mm (W_{b1} = 20 mm, W_{b2} = 30 mm, W_f =25 mm). For Region B, a segmental PZT skin had β = 22.5° and W = 75 mm.

A FE model of the segmental skin (e.g., Region A in Fig. 11(b)) was built using Comsol Multiphysics, as shown

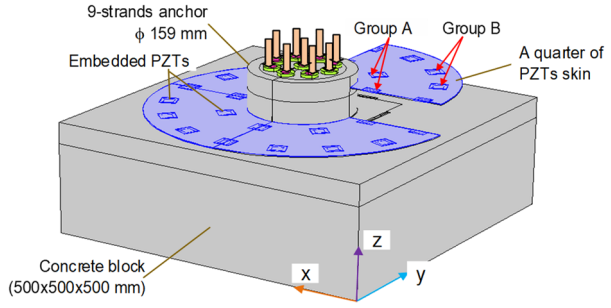

(a) Smart PZT Skin on the anchorage zone

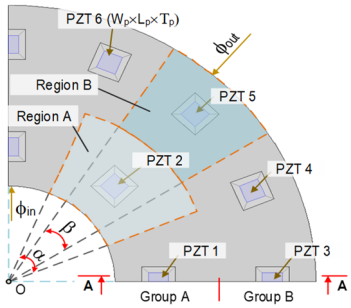

(b) A quarter of PZT Skin

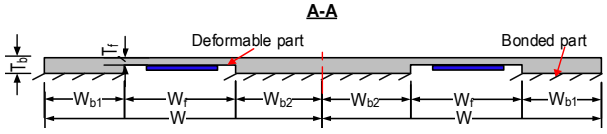

(c) Cross-sectional A-A

Fig. 11 Prototype design of PZT skin for 9-strand anchorage zone

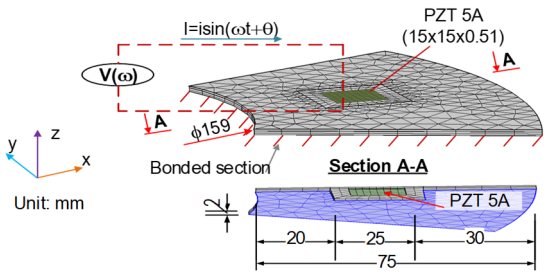

Fig. 12 FE model of a segmental PZT skin (Region A)

in Fig. 12. The meshed FE model consisted of 1046 elements (64 elements for the PZT patch and 982 elements for the skin body). The quadratic hexahedral elements were used for the PZT patch and a flexible part of the skin, and the quadratic tetrahedral elements were used for the bonded part of the skin. The fixed boundary condition was used to simulate the contact surfaces between the anchorage and the skin. For the skin body, aluminum was selected with material properties defined as: E = 70 GPa, ν = 0.33, and ρ = 2700 kg/m^3. Also, PZT 5A was selected as the sensor.

Fig. 13 shows impedance signatures of the segmental PZT skin in the frequency range of 5-45 kHz with 401 sweeping points (under 1V harmonic excitation). There were two distinct resonant impedance peaks, which were Peak 1 (9.3 kHz) and Peak 2 (37.3 kHz). Since the flexible section of the skin had a square shape, the flexural motions with respect to the y-axis were identical to the ones with respect to the x-axis. Impedance responses of Peaks 1-2 were the 1st and 3rd bending motion of the structural plate. With the selected parameters, the frequency range of the PZT skin was predetermined as 5-45 kHz.

4.3 Numerical evaluation of PZT skin for concrete damage detection

4.3.1 FE model of anchorage zone with PZT skin

The FE model of the anchorage zone (described in Section 3.2) was utilized to evaluate the feasibility of the PZT skin for detecting inner concrete damage. Due to the symmetry, a quarter of the anchorage zone was selected for the analysis, as shown in Fig. 14. The quarter of the PZT skin (in Section 4.2) was used to monitor the health condition of the anchorage zone. The orientation of the PZT sensors was designed as illustrated in Fig. 14(b). PZTs 1-2 in (Group A) and PZTs 4-6 (Group B) had 112 mm and 197 mm to the anchor head, respectively. Among six PZTs, PZTs 1-2 had the first and second shortest distances to concrete damage, respectively.

The meshed FE model consisted of 49107 elements which include 384 elements for PZT sensors, 4248 elements for aluminum skin, 2279 elements for the anchorage system, and 42196 elements for the concrete block. The quadratic hexahedral elements were used for the PZT patches, the flexible section of the skin, and the wedges.

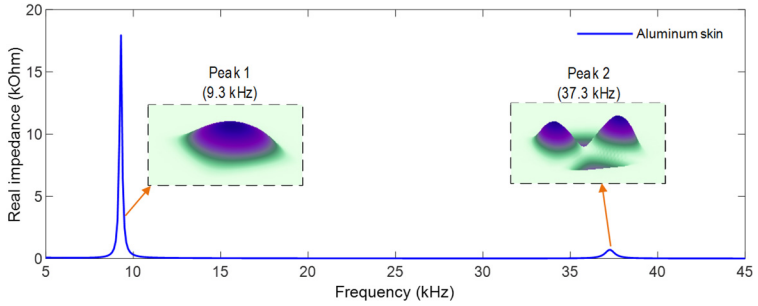

Fig. 13 Impedance responses of PZT skin in the frequency range 5-45 kHz

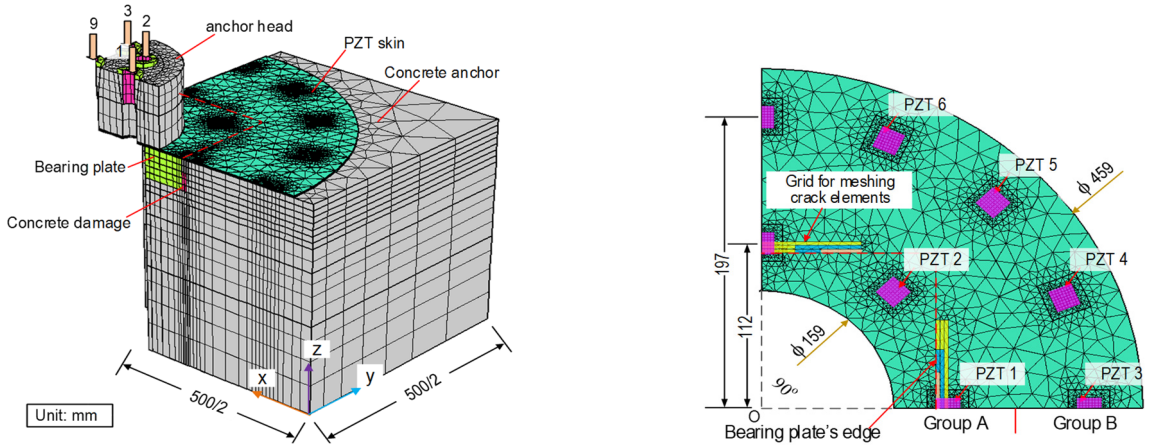

(a) A quarter of anchorage zone (b) A quarter of PZT skin

Fig. 14 FE model of a quarter anchorage zone with PZT skin

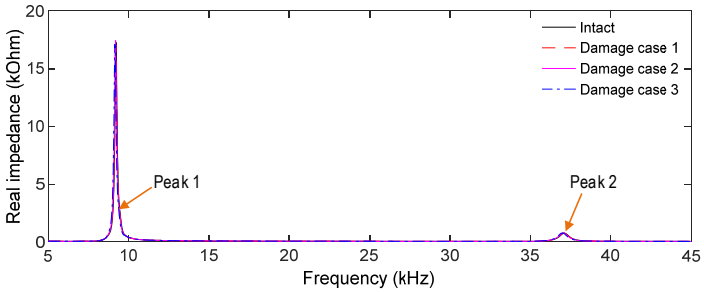

Fig. 15 Impedance responses of PZT 1 skin in the range 5-35 kHz under inner concrete damage cases

Moreover, the quadratic tetrahedral elements were used for the remaining elements. The 3D-spring constants were also used to simulate boundary conditions (as described in Section 2.2). Four simulation scenarios (the intact and three damage cases) were conducted for the FE model, as outlined in Table 3. The impedance responses were acquired in the frequency range of 5-45 kHz under the harmonic voltage of 1V.

4.3.2 Impedance responses of PZT skin

As shown in Fig. 15, the impedance responses of PZT 1 were plotted in the frequency range of 5-45 kHz for the intact and three damage cases. Two resonant impedance peaks (Peaks 1 and 2) exist within the examined frequency range, thereby confirming the predetermination of the PZT skin technique for impedance monitoring.

As shown in Figs. 16(a)-(f), impedance signatures of PZTs 1-6 were zoomed for Peak 1 (8.7-9.7 kHz with 41 sweeping points) and Peak 2 (35.5-38.5 kHz with 31 sweeping points). As shown in the figures, the PZT 1's impedance exhibited the most variation among all six PZT sensors. Impedance signatures of Peak 1 had higher real magnitudes and were more sensitive to concrete damage than those of Peak 2. Notably, under damage case 3, the variations in PZT 1's impedance frequencies were 70 Hz for Peak 1 and 100 Hz for Peak 2. Meanwhile, the variations in impedance frequencies of other PZTs were ignorable.

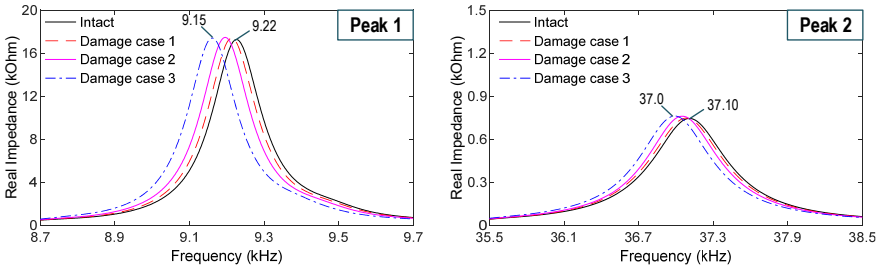

(a) PZT 1

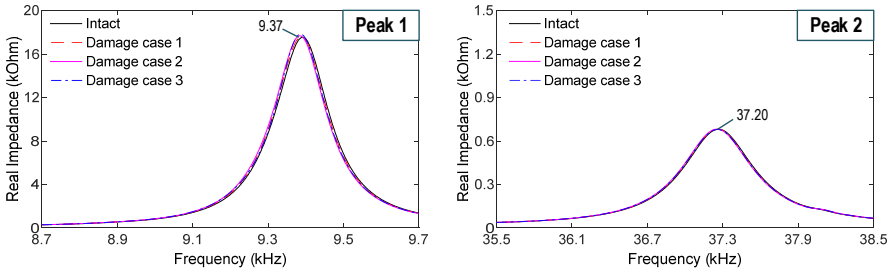

(b) PZT 2

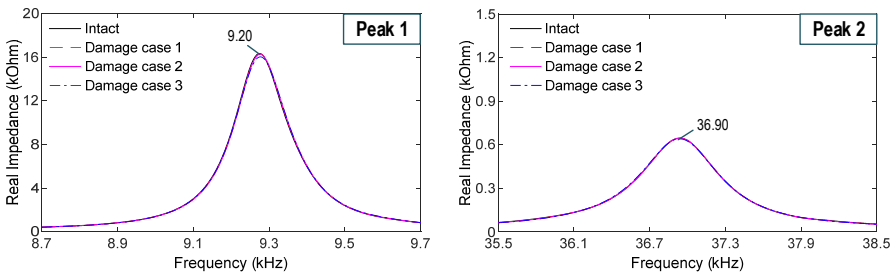

(c) PZT 3

Fig. 16 Impedance signatures of PZTs 1-6 skin under inner concrete damage-induced overloading

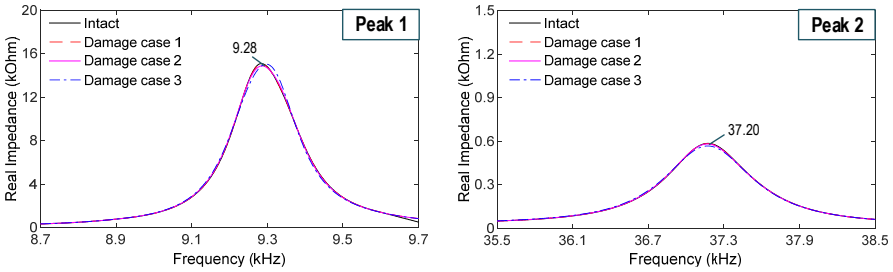

(d) PZT 4

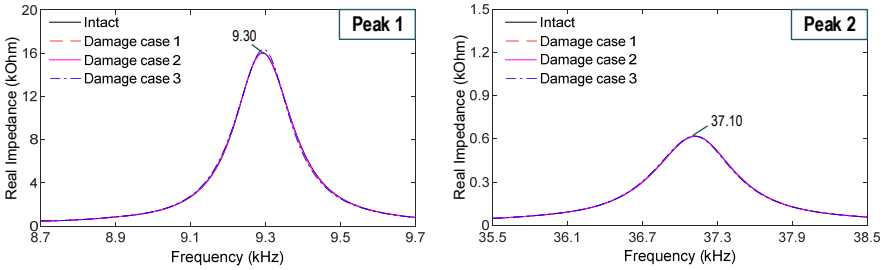

(e) PZT 5

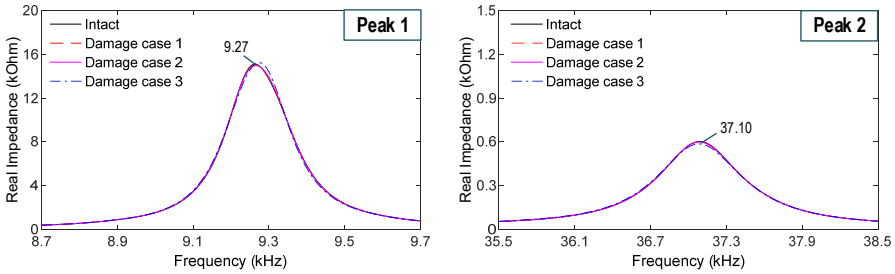

(f) PZT 6

Fig. 16 Continued

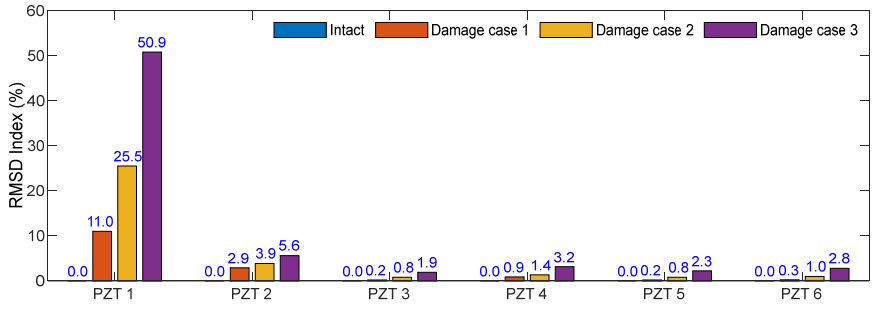

(a) Peak 1's impedance

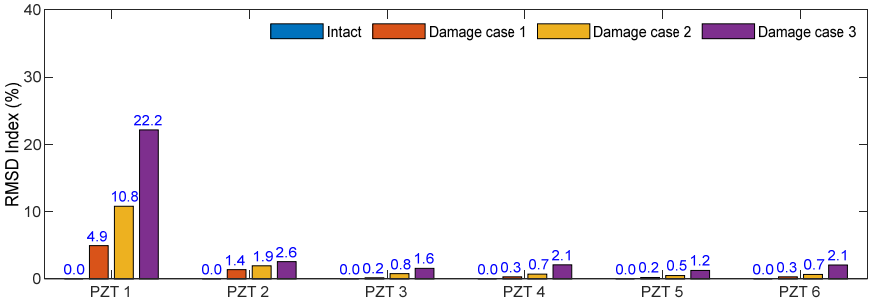

(b) Peak 2's impedance

Fig. 17 RMSD index of impedance signatures of PZTs 1-6 measured via PZT skin

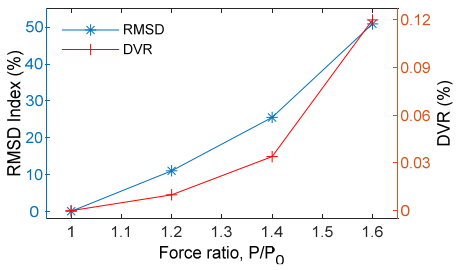

(a) Peak 1's impedance

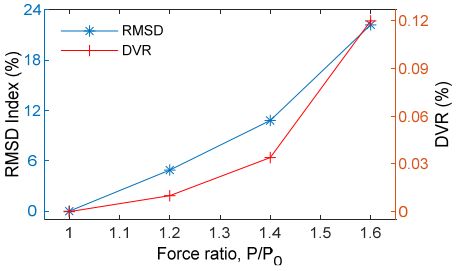

(b) Peak 2's impedance

Fig. 18 Estimation of relative damage severity using numerical impedance features of PZT 1

4.3.3 Inner concrete damage detection using impedance features via PZT skin

The statistical RMSD index was used to compute changes in impedance responses for the frequency ranges of 8.7-9.7 kHz (Peak 1) and 35.5-38.5 kHz (Peak 2) for the intact and three damage cases, as shown in Fig. 17, respectively. The RMSD indices of all PZTs were gradually increased for the damage cases, and the RMSD magnitudes of Peak 1's impedance (see Fig. 17(a)) was more significant than those of Peak 2 (see Fig. 17(b)). Specifically, the observation was made for the RMSD index of Peak 1's impedance. In the intact case, the RSMD indices of all sensors were zero. In damage case 1, the RMSD index of PZT 1 (11.0%) was about 4-11 times larger than that of other PZT sensors. In damage case 2, the RMSD index of PZT 1 (25.5%) was about 6.5-11 times larger than the ones of PZTs 2-6. In damage case 3, the RMSD index of PZT 1 was also the largest value.

4.3.4 Discussion on inner concrete damage detection using impedance features

The impedance features obtained from the direct attachment of PZTs yielded relatively sensitive to the inner concrete damage, and the damage detection result mainly relied on the selecting frequency band. However, since the direct attachment method often leads to high resonant impedance frequencies (> 100 kHz), it demands a high-precision impedance analyzer for the measurement of impedance signatures.

Meanwhile, the impedance responses measured via the PZT skin show higher sensitivity than those measured via the direct attachment method. Also, the frequency range could be predetermined for monitoring impedance signals in practices. The sensitive frequency band was lower than 100 kHz, thus enabling the applicability of the wireless impedance technology for impedance monitoring. From the analysis of PZT skin for impedance monitoring, we observed that (1) the PZT skin technique could be used for detecting the occurrence of damages in the anchorage zone; (2) The location of concrete damage could be indicated by comparing the damage metric of PZTs array, and (3) the magnitude of the RMSD index could be used to alarm the damage severity in the concrete anchorage.

Generally, the RMSD indices can be utilized to estimate relative damage severity in a concrete structure (Zhao *et al.* 2019). To determine the relative damage severity, impedance features of PZT 1 (close to damage zone) was utilized for the calculation. Fig. 18 shows the relationship between the RMSD index and damage volume ratio (DVR) with respect to force ratio P/P_0 for Peaks 1-2' impedance, where P_0 was the design force of prestressing strands (130 kN / strand see Table 3). In the intact state (P/P_0 = 1), the RMSD indices were zero since there was no structural damage. The RMSD indices of Peaks 1-2 were increased due to inner concrete damage-induced overloading events. Also, DVR was nonlinearly increased under prestress force variation, thus demonstrating the nonlinear behavior of the concrete anchorage. As observed in the figure, using RMSD indices for the estimation of damage severity, the result was somewhat larger than the inflict one. It demands a further study on the quantitative assessment of anchorage zone damage.

5. Conclusions

The paper presented the numerical investigation of the PZT skin for impedance measurement sensitive to concrete damage in the prestressed anchorage zone. Firstly, the Ottosen yield criterion for concrete was utilized to analyze the plasticity behavior of the anchorage zone under the compressive loading. Secondly, the damage formations in the concrete of the anchorage zone were analyzed under some overloading cases. Thirdly, the sensitivity analysis of impedance features via surface-mounted PZT sensors to the inner concrete damage was conducted to illustrate the limitations of the conventional impedance monitoring method. Lastly, the novel PZT skin was proposed for the anchorage zone to sensitively monitor the impedance signals of the inner damaged concrete. The feasibility of the proposed method was numerically evaluated for a series of damage cases of the anchorage zone.

The key contribution of the study was the use of PZT skin to detect the locations of severity of damage in the anchorage zone. Since the sensitive frequency ranges of the PZT skin could be predetermined and enhanced, it validated the practicability of the proposed technique for the health monitoring of existing anchorage zones. Moreover, the Ottosen yield criterion for concrete aided to illustrate locations of incipient damage, thus allowing the determination of damage-sensitive impedance sensor placement in the anchorage zones.

While most previous studies on impedance-based concrete damage detection have utilized impedance features

from surface-mounted PZT sensors, this research proposed the PZT skin to enable enhancing impedance features and localizing damage. Despite the promising results, the realistic performance of the PZT skin for integrating structural-impedance responses induced by force variations should be investigated on a real-scale anchorage zone for further study. Moreover, the FE model method should be improved to better simulate the reinforcement in the anchorage zone on the impedance model.

Acknowledgments

This work was supported by Basic Science Research Program through the National Research Foundation of Korea (NRF 2019R1A2B5B01069719). The post-doctoral researcher and graduate students were also supported by the 4th BK21 program of Korean Government.

References

AASHTO (2007), LRFD bridge design specifications, SI units, Washington, DC: American Association of State Highway and Transportation.

Abdullah, A.B.M., Rice, J.A. and Hamilton, H.R. (2015), "Wire breakage detection using relative strain variation in unbonded posttensioning anchors", *J. Bridge Eng.*, **20**(1), 1-12. https://doi.org/10.1061/(ASCE)BE.1943-5592.0000639

Ai, D., Luo, H., Wang, C. and Zhu, H. (2018), "Monitoring of the load-induced RC beam structural tension/compression stress and damage using piezoelectric transducers", *Eng. Struct.*, **154**, 38-51. https://doi.org/10.1016/j.engstruct.2017.10.046

Ai, D., Luo, H. and Zhu, H. (2019), "Numerical and experimental investigation of flexural performance on pre-stressed concrete structures using electromechanical admittance", *Mech. Syst. Signal Process.*, **128**, 244-265. https://doi.org/10.1016/j.ymssp.2019.03.046

Alejano, L.R. and Bobet, A. (2012), *Drucker–prager criterion*, *In The ISRM Suggested Methods for Rock Characterization, Testing and Monitoring*: *2007-2014*, Springer, pp. 247-252. https://doi.org/10.1007/978-3-319-07713-0 (see https://www.springer.com/gp/book/9783319077123)

Bastien, J., Marceau, D., Fafard, M. and Ganz, H.R. (2007), "Use of FEA for design of posttensioning anchor head", *J. Bridge Eng.*, **12**(2), 194-204. https://doi.org/10.1061/(ASCE)1084-0702(2007)12:2(194)

Breen, J.E. (1994), Anchorage zone reinforcement for post-tensioned concrete girders, Transportation Research Board. (https://trid.trb.org/view/388973)

Cervenka, V. and Ganz, H.R. (2014), "Validation of post-tensioning anchorage zones by laboratory testing and numerical simulation", *Struct. Concrete*, **15**(2), 258-268. https://doi.org/10.1002/suco.201300038

Chang, Y.F., Chen, Y.H., Sheu, M.S. and Yao, G.C. (2006), "Residual stress–strain relationship for concrete after exposure to high temperatures", *Cement Concrete Res.*, **36**(10), 1999-2005. https://doi.org/10.1016/j.cemconres.2006.05.029

Chauthoi620 (2018), Dam I, (Accessed on, May 7, 2018). https://620chauthoi.com/san-pham/dam-i33/

Dang, N.L., Huynh, T.C. and Kim, J.T. (2019), "Local strand-breakage detection in multi-strand anchorage system using an impedance-based stress monitoring method-feasibility study", *Sensors*, **19**(5). https://doi.org/10.3390/s19051054

Dang, N.L., Huynh, T.C., Pham, Q.Q., Lee, S.Y. and Kim, J.T. (2020a), "Damage-sensitive impedance sensor placement on multi-strand anchorage based on local stress variation analysis", *Struct. Control Health Monitor.*, **27**, e2547. https://doi.org/10.1002/stc.2547

Dang, N.L., Pham, Q.Q. and Kim, J.T. (2020b), "Piezoelectric-based hoop-type interface for impedance monitoring of local strand breakage in prestressed multi-strand anchorage", *Struct. Control Health Monitor.*, **28**(1). https://doi.org/10.1002/stc.2649

Darwin, D., Dolan, C.W. and Nilson, A.H. (2016), *Design of Concrete Structures*, McGraw-Hill Education, New York.

Dragon, A., Halm, D. and Désoyer, T. (2000), "Anisotropic damage in quasi-brittle solids: modelling, computational issues and applications", *Comput. Methods Appl. Mech. Eng.*, **183**(3-4), 331-352. https://doi.org/10.1016/S0045-7825(99)00225-X

Eringen, A.C., Speziale, C. and Kim, B. (1977), "Crack-tip problem in non-local elasticity", *J. Mech. Phys. Solids*, **25**(5), 339-355. https://doi.org/10.1016/0022-5096(77)90002-3

Grosse, C.U. (2009), "Acoustic emission localization methods for large structures based on beam forming and array techniques", *Proceedings of the NDTCE*, 9.

Guyon, Y. (1974), *Limit-State Design of Prestressed Concrete*, John Wiley & Sons.

He, Z.Q. and Liu, Z. (2010), "Optimal three-dimensional strut-and-tie models for anchorage diaphragms in externally prestressed bridges", *Eng. Struct.*, **32**(8), 2057-2064. https://doi.org/10.1016/j.engstruct.2010.03.006

Henault, J.M., Quiertant, M., Delepine-Lesoille, S., Salin, J., Moreau, G., Taillade, F. and Benzarti, K. (2012), "Quantitative strain measurement and crack detection in RC structures using a truly distributed fiber optic sensing system", *Constr. Build. Mater.*, **37**, 916-923. https://doi.org/10.1016/j.conbuildmat.2012.05.029

Hofstetter, B.V.G. (2013), "Review and enhancement of 3D concrete models for large-scale numerical simulations of concrete structures", *Int. J. Numer. Anal. Methods Geomech.*, **37**(3), 221-246. https://doi.org/10.1002/nag.1096

Hou, D.W., Zhao, J.L., Shen, J.S.L. and Chen, J. (2017), "Investigation and improvement of strut-and-tie model for design of end anchorage zone in post-tensioned concrete structure", *Constr. Build. Mater.*, **136**, 482-494. https://doi.org/10.1016/j.conbuildmat.2017.01.033

Huynh, T.C. and Kim, J.T. (2017a), "Quantitative damage identification in tendon anchorage via PZT interface-based impedance monitoring technique", *Smart Struct. Syst.*, *Int. J.*, **20**(2), 181-195. https://doi.org/10.12989/sss.2017.20.2.181

Huynh, T.C. and Kim, J.T. (2017b), "Quantification of temperature effect on impedance monitoring via PZT interface for prestressed tendon anchorage", *Smart Mater. Struct.*, **26**(12), 1-19. https://doi.org/10.1088/1361-665X/aa931b

Huynh, T.C., Lee, K.S. and Kim, J.T. (2015), "Local dynamic characteristics of PZT impedance interface on tendon anchorage under prestress force variation", *Smart Struct. Syst.*, *Int. J.*, **15**(2), 375-393. https://doi.org/10.12989/sss.2015.15.2.375

Huynh, T.C., Park, J.H., Jung, H.J. and Kim, J.T. (2019), "Quasi-autonomous bolt-loosening detection method using vision-based deep learning and image processing", *Automat. Constr.*, **105**. https://doi.org/10.1016/j.autcon.2019.102844

Jang, K., Kim, N. and An, Y.K. (2019), "Deep learning–based autonomous concrete crack evaluation through hybrid image scanning", *Struct. Health Monitor.*, **18**(5-6), 1722-1737. https://doi.org/10.1177/1475921718821719

Jang, K., An, Y.K., Kim, B. and Cho, S. (2020), "Automated crack evaluation of a high-rise bridge pier using a ring-type climbing robot", *Comput.-Aided Civil Infrastruct. Eng.*, **36**(1). https://doi.org/10.1111/mice.12550

Jefferson, A.D., Mihai, I.C., Tenchev, R., Alnaas, W.F., Cole, G. and Lyons, P. (2016), "A plastic-damage-contact constitutive

model for concrete with smoothed evolution functions", *Comput. Struct.*, **169**, 40-56. https://doi.org/10.1016/j.compstruc.2016.02.008

Kang, D., Benipal, S.S., Gopal, D.L. and Cha, Y.J. (2020), "Hybrid pixel-level concrete crack segmentation and quantification across complex backgrounds using deep learning", *Automat. Constr.*, **118**. https://doi.org/10.1016/j.autcon.2020.103291

Kim, J.T. and Stubbs, N. (2003), "Crack detection in beam-type structures using frequency data", *J. Sound Vib.*, **259**(1), 145-160. https://doi.org/10.1006/jsvi.2002.5132

Kim, J.T., Park, J.H., Hong, D.S. and Park, W.S. (2010), "Hybrid health monitoring of prestressed concrete girder bridges by sequential vibration-impedance approaches", *Eng. Struct.*, **32**(1), 115-128. https://doi.org/10.1016/j.engstruct.2009.08.021

Kupfer, H., Hilsdorf, H.K. and Rusch, H. (1969), "Behavior of concrete under biaxial stresses", *Journal Proceedings*.

Lee, J. and Fenves, G.L. (1998), "Plastic-damage model for cyclic loading of concrete structures", *J. Eng. Mech.*, **124**(8), 892-900. https://doi.org/10.1061/(ASCE)0733-9399(1998)124:8(892)

Lee, S. and Kalos, N. (2014), "Non-destructive testing methods in the US for bridge inspection and maintenance", *KSCE J. Civil Eng.*, **18**(5), 1322-1331. https://doi.org/10.1007/s12205-014-0633-9

Liang, C., Sun, F. and Rogers, C.A. (1996), "Electro-mechanical impedance modeling of active material systems", *Smart Mater. Struct.*, **5**(2), 171-186. https://doi.org/10.1088/0964-1726/5/2/006

Lim, Y.Y. and Soh, C.K. (2012), "Effect of varying axial load under fixed boundary condition on admittance signatures of electromechanical impedance technique", *J. Intell. Mater. Syst. Struct.*, **23**(7), 815-826. https://doi.org/10.1177/1045389X12437888

Loutridis, S., Douka, E. and Hadjileontiadis, L.J. (2005), "Forced vibration behaviour and crack detection of cracked beams using instantaneous frequency", *NDT & E Int.*, **38**(5), 411-419. https://doi.org/10.1016/j.ndteint.2004.11.004

Lu, X., Lim, Y.Y. and Soh, C.K. (2017), "A novel electromechanical impedance–based model for strength development monitoring of cementitious materials", *Struct. Health Monitor.*, **17**(4), 902-918. https://doi.org/10.1177/1475921717725028

Mazars, J. and Pijaudier-Cabot, G. (1989), "Continuum damage theory—application to concrete", *J. Eng. Mech.*, **115**(2), 345-365. https://doi.org/10.1061/(ASCE)0733-9399(1989)115:2(345)

Mehrabi, A.B., Ligozio, C.A., Ciolko, A.T. and Wyatt, S.T. (2010), "Evaluation, rehabilitation planning, and stay-cable replacement design for the hale boggs bridge in Luling, Louisiana", *J. Bridge Eng.*, **15**(4), 364-372. https://doi.org/10.1061/(ASCE)BE.1943-5592.0000061

Min, J., Yun, C.B. and Hong, J.W. (2016), "An electromechanical impedance-based method for tensile force estimation and damage diagnosis of post-tensioning systems", *Smart Struct. Syst.*, *Int. J.*, **17**(1), 107-122. https://doi.org/10.12989/sss.2016.17.1.107

Nawy, E.G. (2010), *Prestressed Concrete*: *A Fundamental Approach*, Prentice Hall.

Okumus, P. and Oliva, M.G. (2013), "Evaluation of crack control methods for end zone cracking in prestressed concrete bridge girders", *PCI Journal*, **58**(2). https://doi.org/10.15554/pcij.03012013.91.105

Ottosen, N.S. (1977), "A failure criterion for concrete", *J. Eng. Mech. Div.*, **103**(4), 527-535. https://doi.org/10.1061/JMCEA3.0002248

Ottosen, N.S. and Ristinmaa, M. (2005), *The mechanics of constitutive modeling*, Elsevier.

Papanikolaou, V.K. and Kappos, A.J. (2007), "Confinement-sensitive plasticity constitutive model for concrete in triaxial compression", *Int. J. Solids Struct.*, **44**(21), 7021-7048. https://doi.org/10.1016/j.ijsolstr.2007.03.022

Park, J.H., Kim, J.T., Ryu, Y.S. and Lee, J.M. (2007), "Monitoring cracks and prestress-loss in PSC girder bridges using vibration-based damage detection techniques", In: *Health Monitoring of Structural and Biological Systems 2007*, International Society for Optics and Photonics. https://doi.org/10.1117/12.720907

Park, H.J., Sohn, H., Yun, C.B., Chung, J. and Lee, M.M.S. (2012), "Wireless guided wave and impedance measurement using laser and piezoelectric transducers", *Smart Mater. Struct.*, **21**(3). https://doi.org/10.1088/0964-1726/21/3/035029

Putcha, C., Dutta, S. and Rodriguez, J. (2020), "Risk priority number for bridge failures", *Practice Period. Struct. Des. Constr.*, **25**(2), 04020010. https://doi.org/10.1061/(ASCE)SC.1943-5576.0000480

Ro, K.M., Kim, M.S. and Lee, Y.H. (2020), "Validity of Anchorage Zone Design for Post-Tensioned Concrete Members with High-Strength Strands", *Appl. Sci.*, **10**(9). https://doi.org/10.3390/app10093039

Roberts, C. (1990), "Behavior and design of the local anchorage zone in post-tensioned concrete", Thesis; The University of Texas, Austin, TX, USA.

Ryu, J.Y., Huynh, T.C. and Kim, J.T. (2018), "Tension force estimation in axially loaded members using wearable piezoelectric interface technique", *Sensors*, **19**(1), 1-17. https://doi.org/10.3390/s19010047

Schneider, U. (1976), "Behaviour of concrete under thermal steady state and non-steady state conditions", *Fire Materials*, **1**(3), 103-115. https://doi.org/10.1002/fam.810010305

Vilppo, J., Kouhia, R., Hartikainen, J., Kolari, K., Fedoroff, A. and Calonius, K. (2021), "Anisotropic damage model for concrete and other quasi-brittle materials", *Int. J. Solids Struct.*, **225**. https://doi.org/10.1016/j.ijsolstr.2021.111048

VSL (20180, VSL Strand Post-tensioning systems. Available online (accessed on 12 June 2018): http://www.daorenc.com/kr/wp-content/uploads/2016/05/pt.pdf

Wu, J., Xian, G. and Li, H. (2018), "A novel anchorage system for CFRP cable: Experimental and numerical investigation", *Compos. Struct.*, **194**, 555-563. https://doi.org/10.1016/j.compstruct.2018.04.006

Xia, Y., Langelaar, M. and Hendriks, M.a.N. (2020), "A critical evaluation of topology optimization results for strut-and-tie modeling of reinforced concrete", *Comput.-Aided Civil Infrastruct. Eng.*, **35**(8), 850-869. https://doi.org/10.1111/mice.12537

Yaghoubi, S.T., Kouhia, R., Hartikainen, J. and Kolari, K. (2014), "A continuum damage model based on ottosen's four parameter failure criterion for concrete", *J. Struct. Mech.*, **47**, 50-60.

Yang, Y., Hu, Y. and Lu, Y. (2008), "Sensitivity of PZT impedance sensors for damage detection of concrete structures", *Sensors*, **8**(1), 327-346. https://doi.org/10.3390/s8010327

Yao, Y., Tung, S.T.E. and Glisic, B. (2014), "Crack detection and characterization techniques-An overview", *Struct. Control Health Monitor.*, **21**(12), 1387-1413. https://doi.org/10.1002/stc.1655

Zhang, C., Yan, Q., Panda, G.P., Wu, W., Song, G. and Vipulanandan, C. (2020a), "Real-time monitoring stiffness degradation of hardened cement paste under uniaxial compression loading through piezoceramic-based electromechanical impedance method", *Constr. Build. Mater.*, **256**. https://doi.org/10.1016/j.conbuildmat.2020.119395

Zhang, X., Wu, H., Li, J., Pi, A. and Huang, F. (2020b), "A constitutive model of concrete based on Ottosen yield criterion", *Int. J. Solids Struct.*, **193-194**, 79-89. https://doi.org/10.1016/j.ijsolstr.2020.02.013

Zhao, S., Fan, S. and Chen, J. (2019), "Quantitative assessment of

the concrete gravity dam damage under earthquake excitation using electro-mechanical impedance measurements", *Eng. Struct.*, **191**, 162-178. https://doi.org/10.1016/j.engstruct.2019.04.061

CC